

# Chaos in one-dimensional lattices under intense laser fields

M. A. M. de Aguiar<sup>a</sup>, H. S. Brandi<sup>b</sup>, Belita Koiller<sup>b</sup>, and Eduardo R. Mucciolo<sup>c</sup>

<sup>a</sup> *Instituto de Física, Universidade Estadual de Campinas,*

*Cx. P. 6165, 13083-970, São Paulo, Brazil*

<sup>b</sup> *Instituto de Física, Universidade Federal do Rio de Janeiro,*

*Cx. P. 68.528, 21945-970, Rio de Janeiro, Brazil*

<sup>c</sup> *Departamento de Física, Pontifícia Universidade Católica do Rio de Janeiro,*

*Cx. P. 38071, 22452-970, Rio de Janeiro, Brazil*

(April 24, 2013)

## Abstract

A model is investigated where a monochromatic, spatially homogeneous laser field interacts with an electron in a one-dimensional periodic lattice. The classical Hamiltonian is presented and the technique of stroboscopic maps is used to study the dynamical behavior of the model. The electron motion is found to be completely regular only for small field amplitudes, developing a larger chaotic region as the amplitude increases. The quantum counterpart of the classical Hamiltonian is derived. Exact numerical diagonalizations show the existence of universal, random-matrix fluctuations in the electronic energy bands dressed by the laser field. A detailed analysis of the classical phase space is compatible with the statistical spectral analysis of the quantum model. The application of this model to describe transport and optical absorption in semiconductor superlattices submitted to intense infrared laser radiation is proposed.

78.90.+t, 05.45.+b

## I. INTRODUCTION

The search for systems whose dynamical behavior can be fine tuned by one or more external parameters has been an important activity in the field of chaos in the last decades [1]. The kicked rotor [2] has emerged as the paradigm model of a periodically driven system whose motion depends strongly on the strength of the external perturbation. The study of this particular model allowed us to understand phenomena such as the dynamical localization of atoms interacting with microwave radiation in an optical trap [3].

For time-independent, Hamiltonian systems, one has also extensively searched for situations where the dynamics is a sensitive function of a *single* parameter. Common situations occur when two integrable potentials are coupled to form a nonintegrable system. One case of particular interest, both theoretically and experimentally, is the hydrogen atom in the presence of a uniform magnetic field [4], since the limiting cases of zero magnetic field and zero Coulomb force are exactly solvable.

In this work we study a model describing the motion of an electron in a one-dimensional periodic potential in the presence of an external monochromatic laser field. The most accessible experimental realization of this model occurs in semiconductor superlattices (multiple quantum-well structures) irradiated with intense infrared laser pulses.

We have considered a one-dimensional time-periodic effective classical Hamiltonian describing the interaction of an intense laser field with an electron in a 1-D periodic lattice. We show that the effective Hamiltonian is *integrable* in the limiting case of zero field strength. As the field strength becomes larger, the behavior of the classical orbits become increasingly chaotic. For strong fields the Hamiltonian is invariant under a scaling transformation involving the electron momentum, the average energy of the Hamiltonian, and the field strength. Therefore, to understand the whole range of laser intensities it is necessary only to study the weak and intermediate field regimes.

In order to propose a physical realization of this model situation we have studied the quantum counterpart of the classical Hamiltonian. Through numerical simulations, we found that typical signatures of quantum chaos, such as level repulsion and spectral rigidity, are present for intermediate and large values of field strengths. Based on the energy level statistics observed, it was possible to identify a weak (Poisson) and a strong (Wigner-Dyson) level correlation regime as the laser intensity increases. The statistical spectral analysis approach, which provides strong evidence of chaotic and regular behaviors, can be completely understood in the light of the classical model.

This paper is organized as follows. In Sec. II we present the classical model and study the dynamics of the system as a function of the laser field strength using the technique of stroboscopic maps. In Sec. III we derive the quantum model and compare the classical results. A discussion on possible experimental observations is given in Sec. IV. Finally, Sec. V is dedicated to the conclusions.

## II. THE CLASSICAL MODEL

Consider the Hamiltonian describing an electron in a 1-D periodic potential under the action of an applied homogeneous monochromatic laser field. The laser field can be represented

by a time-dependent vector potential (in the dipole approximation) minimally coupled to the electron. In this limit, the laser field is not affected by the electron motion and the vector potential acts as a time-periodic external force. The lattice potential is periodic and can be written in terms of a sum over reciprocal vectors  $G_\ell = 2\pi\ell/d$ , with  $d$  denoting the lattice constant and  $\ell = 0, \pm 1, \pm 2, \dots$ . Explicitly,

$$H(p, q) = \frac{1}{2m} \left[ p - \frac{e}{c} A_0 \cos(\omega t) \right]^2 - 2 \sum_{\ell=1}^{\infty} \sigma_\ell \cos(\ell G_1 q). \quad (1)$$

The term proportional to  $A_0^2$  in  $H$  yields a pure time-dependent factor that does not affect the equations of motion of the electron. Therefore, this term can be eliminated and the classical motion can be obtained from the effective Hamiltonian

$$H_{\text{eff}}(p, q) = \frac{p^2}{2m} - 2 \sum_{\ell=1}^{\infty} \sigma_\ell \cos(\ell G_1 q) + \frac{eA_0 p}{mc} \cos(\omega t). \quad (2)$$

In order to compare the results of the classical calculations with the quantum analysis shown below, we first introduce suitable energy and frequency scales into the problem:  $\epsilon \equiv \hbar^2 G_1^2 / 2m$  and  $\hbar\omega = \epsilon\omega_0$ , such that the dimensionless lattice potential strength becomes  $\sigma_\ell^0 \equiv \sigma_\ell/\epsilon$ . This naturally leads to a new pair of canonically conjugate variables

$$P = \frac{\hbar}{\sqrt{m\epsilon}} p$$

and

$$Q = \frac{\sqrt{m\epsilon}}{\hbar} q$$

and a new time scale  $\tau \equiv \epsilon t/\hbar$ . The resulting equations of motion for  $P(\tau)$  and  $Q(\tau)$  can be derived from the rescaled Hamiltonian

$$\mathcal{H}(P, Q) = \frac{(P/\hbar)^2}{2} - 2 \sum_{\ell=1}^{\infty} \sigma_\ell^0 \cos(\ell \sqrt{2}Q) + \frac{x\omega_0(P/\hbar)}{\sqrt{2}} \cos(\omega_0\tau), \quad (3)$$

where  $x \equiv eA_0 G_1 / \omega mc$ . The total energy associated to the effective Hamiltonian in Eq. (2) is related to the rescaled (dimensionless) energy  $\mathcal{E}(\tau)$  by  $E_{\text{eff}}(t) = \epsilon \mathcal{E}(\epsilon t/\hbar)$ . The dimensionless parameter  $x$  characterizes the laser intensity. For numerical estimates, it can be expressed in the more appropriate form

$$x = \left( \frac{\lambda}{d} \right) \sqrt{\frac{n_r I}{I_C}}, \quad (4)$$

with  $I = n_r \omega^2 A_0^2 / 8\pi c$  and  $n_r$  denoting the refraction index of the medium. The quantity  $I_C = m^2 \omega^2 c^3 / 8\pi e^2$  is the Compton intensity, i.e.,  $I_C = 1.37 \times 10^{18} \times \lambda^{-2}$  [W/cm<sup>2</sup>], with the laser wavelength  $\lambda$  given in  $\mu\text{m}$ .

Since the potential is a periodic function of  $Q$ ,  $Q$  and  $P$  are *angle* and *action* variables, respectively, with  $P$  having units of  $\hbar$ . Thus, hereafter, we shall drop the  $\hbar$  in Eq. (3) and

understand that  $P$  is measured in units of  $\hbar$ . We shall also restrict  $Q$  to the primitive cell interval  $-\pi/\sqrt{2}$  to  $\pi/\sqrt{2}$ .

In order to carry out our analysis, we will consider only the first three reciprocal components of the periodic lattice potential in Eq. (3). There is nothing special about this choice and it just represents a possible truncation of the well-known Kronig-Pennig potential. The number of components is taken to be relatively small in order to facilitate the numerical simulations; at the same time, it is also sufficiently large to allow for the existence of a nontrivial classical dynamics. For similar reasons, in all numerical calculations (classical and quantum) in this work we shall adopt  $\sigma_\ell^0 = \sigma^0 = 0.25$  (for  $-3 \leq \ell \leq 3$ ) and  $\omega_0 = 0.3$ .

Figure 1 displays *stroboscopic maps* for the classical system defined by Eq. (3) at different laser intensities. These maps are generated by plotting the coordinates  $Q$  and  $P$  at discrete times  $\tau_n = 2\pi n/\omega_0$ ,  $n = 0, 1, 2, \dots$ , producing a sequence of points  $(Q_n, P_n)$ . Each initial condition  $(Q_0, P_0)$  gives rise to a different sequence. If these points fall on a one-dimensional curve, the trajectory lies on a cylinder in the extended  $(Q, P, \tau)$  phase space and is said to be regular. If, on the other hand, the points cover a two-dimensional area of the  $QP$  plane, the trajectory is said to be irregular or chaotic. Figure 2 shows contour levels of the Hamiltonian for  $x = 0$ .

Let us now discuss the classical motion arising from Eq. (3) in terms of stroboscopic maps for different laser intensities. For  $x = 0$ , Figure 1(a), the map is integrable and all points lie on 1-D curves. The wells centered at  $Q = P = 0$  and  $P = 0$ ,  $Q \simeq \pm 1.5$ , trap low-energy electrons, whereas those with higher energies, above or below these trapping *islands*, move along the lattice from left to right (positive  $P$ ) or from right to left (negative  $P$ ). These trajectories are clearly related to the conduction properties of the material. In Figure 2 the numbers close to the curves indicate the value of  $\mathcal{E}$ . For  $x \neq 0$ , only average energies can be defined: above the islands, they are roughly equal to the kinetic term alone, since the other terms have an oscillatory behavior.

For slightly larger intensities, a small amount of chaos begins to permeate the region where the separatrices involving the islands used to be. This effect is clearly visible in Figure 1(b), where  $x = 1$ . In the new chaotic zone, the electromagnetic field *shakes* the electron, forcing it to move in opposite directions intermittently, inhibiting charge transport through the crystal. Figure 3 shows typical electron trajectories for chaotic (lower curve) and regular (upper curve) regimes when  $x = 1$ . These trajectories are related to different initial conditions. Note that the chaotic trajectory is restricted to a narrower range of  $Q$ -values in comparison to the regular trajectory, which extends over a much wider  $Q$  region.

For  $x = 10$ , Fig. 1(c), a rather large chaotic zone develops at  $|P| \lesssim 3.5$ . Figure 1(d) shows that for  $x = 100$ , the region close to  $|P| = 0$  becomes dominated by chaotic trajectories. Notice that the maps for  $x = 10$  and  $x = 100$  are almost identical at large  $|P|$ . This is due to the existence of a *quasi* scaling law in the classical motion: For  $x \gg 1$ , one can discard the periodic potential and change  $P \rightarrow \alpha P$  and  $x \rightarrow \alpha x$ , rescaling  $\mathcal{E} \rightarrow \alpha^2 \mathcal{E}$ . As a consequence, it is possible to infer that for very strong field intensities the regime will be predominantly chaotic, even at (relatively) low energies.

From the figures and the equations of motion, for any given value of  $x$ , it is easy to see that  $P$  tends to a constant, provided its initial value is sufficiently large. Moreover, at  $x = 0$  the average energy also becomes equal to a constant since the average of the coupling term becomes negligible. The small  $P$  region, on the other hand, is largely affected by the

electromagnetic field and the lattice potential if  $x$  is not too small.

### III. THE QUANTUM MODEL

The quantum Hamiltonian corresponding to the classical model of the previous section can be written in the form

$$H = H_k + H_{\text{int}}, \quad (5)$$

where

$$\begin{aligned} H_k &= \frac{p^2}{2m} - 2 \sum_{\ell=1}^3 \sigma_{\ell} \cos(\ell G_1 q) \\ &= -\frac{\hbar^2}{2m} \left( \frac{d}{dq} + ik \right)^2 - 2 \sum_{\ell=1}^3 \sigma_{\ell} \cos(\ell G_1 q) \end{aligned} \quad (6)$$

and

$$H_{\text{int}} = \frac{e}{mc} A(t)p + \frac{e^2}{2mc^2} A(t)^2, \quad (7)$$

with

$$A(t) = A_0 \cos \omega t \quad (8)$$

(notice that  $m$  here is the free electron mass). In these equations we have used Bloch's theorem to decouple the Hamiltonian into reduced components, which we denote by the label  $k$ . We can transform  $H$  into a Floquet Hamiltonian  $H_F$  by using as a basis the eigenstates  $|\ell, n\rangle \equiv |G_{\ell} + k, n\rangle$ . The Bloch-Floquet states fully incorporate the symmetries of the original Hamiltonian:  $G$  and  $n$  are associate to the discrete space translations of the lattice vectors and time translations of the vector potential, respectively. One can then show [5,6] that the spectrum of  $H$  follows from the diagonalization of the Bloch-Floquet matrix

$$\langle \ell', n' | H_F | \ell, n \rangle = \left[ n\hbar\omega + \frac{\hbar^2(G_{\ell} + k)^2}{2m} \right] \delta_{\ell, \ell'} \delta_{n, n'} + J_{n'-n} \left( \frac{eA_0}{\omega mc} (G_{\ell} - G_{\ell'}) \right) \sigma_{\ell-\ell'}, \quad (9)$$

where  $J_n$  is the Bessel function of order  $n$  and  $\sigma_{\ell} = \sigma$  for  $-3 \leq \ell \leq 3$ , and zero otherwise. The eigenvalues of the Floquet Hamiltonian are quasi-energies but, for simplicity, will be referred to as energies. The units and conventions are the same as those defined in Sec. II.

We carry out quantum calculations considering a plane-wave basis set with a finite number of  $G_{\ell}$ :  $-\ell_{\text{max}} \leq \ell \leq \ell_{\text{max}}$ , which leads to a  $(2\ell_{\text{max}} + 1)$ -band model in the absence of the laser field. We take  $\ell_{\text{max}} = 3$  in most calculations presented below, which corresponds to a seven-band model. The choice of a finite number of bands to describe a real crystal is justified, since highly excited bands (differing from the Fermi level by an amount larger than the work function of the material) can never be accessed due to the photoelectric effect. In the absence of the laser field, the electronic energy levels of (5) consist essentially

of the free-electron parabola folded into the first Brillouin zone, plus gaps opening at the crossing points ( $k = 0$  and  $\pm G_1/2$ ). Inclusion of the laser field produces a dressing effect in the bands, which may be described by replica bands translated by  $n\omega_0$  for integer values of  $n$ . The values adopted for  $\sigma^0$  and  $\omega_0$  are such as to strongly mix the replicas forming the dressed bands. The interaction  $H_{\text{int}}$  causes an anticrossing whenever two noninteracting replica bands cross. Our calculations also involve truncation of the basis set into a finite number of  $n$ -values:  $|n| \leq n_{\text{max}}$ . The value of  $n_{\text{max}}$  is chosen such as to guarantee the completeness of the replica-bands within the energy range of interest, and consequently convergence in the calculation of spectral properties (see discussion below).

Figure 4 shows the dressed bands spectrum for the energy range  $1 < E < 5$  at  $x = 0$ ,  $x = 1$ , and  $x = 10$  (as mentioned before, in a real situation the appropriate range of energy would be defined by the Fermi energy and the work function of the material). For this energy range,  $n_{\text{max}} = 40$  is sufficient to achieve saturation in the replicas. For  $x = 0$  no level repulsion is observed while for  $x = 1$  some structure in the energy bands is clearly identified. For  $x = 10$  the spectrum reveals an intricate level repulsion structure which resembles those characteristic of quantum chaotic regimes in other systems [1]. All the main features of the classical stroboscopic map can be inferred from these spectra. For all energies we can observe that, as  $x$  increases, the anticrossing and enhanced level repulsion among the electronic bands leads to narrower minibands. From elementary band theory, narrow bands are always associated to poor transport properties. For example, in a standard tight-binding scenario, the band width is proportional to the hopping matrix element between atomic orbitals (equivalent to Wannier functions in the present plane-waves description) centered at neighboring lattice sites. Smaller values of this hopping element indicate a tendency towards localization, which, in the corresponding classical motion, appears as trajectories confined to a narrower range of  $Q$  values (recall similar discussion in Sec. II with respect to Fig. 3).

These trends are confirmed by a quantitative analysis of the spectral fluctuations. We recall [1] that weak and strong interlevel correlations have been associated with classically regular and chaotic behaviors, respectively. The latter is usually described at the quantum level by the Gaussian ensembles of random matrix theory [7]. In Figure 5 we present the distribution of nearest-neighbor level spacings (NNS) obtained for increasing values of the field intensity parameter  $x$ , with bands confined to the energy interval 1 to 5. For  $x = 0$  [Figure 5(a)] the NNS distribution is very close to an exponential (the Poisson law), demonstrating the lack of short-range correlation between levels. The corresponding classical momentum varies roughly from -3 to 3 for this energy interval. For  $x = 1$  [Figure 5(b)] a crossover regime appears in which the NNS is neither Poissonian nor GOE-like [8]. However, for  $x = 10$  [Figure 5(c)] the Wigner surmise provides a very accurate fit, as expected from the classical analysis. The curves obtained for the least square deviation  $\Delta_3$  [7] (not shown) lead to a similar interpretation with respect to large-range correlations.

We now discuss the robustness of our results with respect to the basis set truncation, i.e., the influence of the cutoff parameters defining the range of  $\ell$  and  $n$  values in the calculations presented above. Figure 6 presents the NNS for  $x = 10$ . Figure 6(a) is obtained considering a plane-waves basis cutoff for  $\ell_{\text{max}} = 1$ , while Figure 6(b) refers to  $\ell_{\text{max}} = 5$ . Note that the results in (a) and (b) are essentially the same, and also very similar to Figure 5(c), illustrating that the plane-wave basis cutoff is not a relevant parameter. This fact supports that the

conclusions drawn from our model, where only a finite number of bands is incorporated, should be applicable to real experiments. For a given energy range,  $n_{\max}$  must be taken sufficiently large to guarantee convergence. Since, in the absence of the laser field, the full spectrum associated to larger values of  $\ell_{\max}$  covers a wider range of energies, the adopted value of  $n_{\max}$  increases with  $\ell_{\max}$ . Thus  $n_{\max} = 60$  is required if we consider  $\ell_{\max} = 5$ , while for  $\ell_{\max} = 3$ ,  $n_{\max} = 40$  already leads to converged results. The results presented in Figure 6 show that the choice of the basis set cutoff parameters must take into account the energy range of physical interest. Our main conclusions about the system dynamics inferred from the quantum simulations are well understood from the classical analysis. Therefore, quantum and classical results are completely compatible.

#### IV. EXPERIMENTAL ASPECTS

The scheme proposed here is suitable to model the physics of high-quality semiconductor vertical superlattices in the presence of intense monochromatic light radiation [10]. In order to make the connection we replace the one-dimensional potential by the superlattice potential. It would not be computationally harder to introduce a few more reciprocal components to obtain a  $V(q)$  in closer resemblance to that of a superlattice. We found, however, that increasing the number of components did not change our results qualitatively. Thus, the only necessary (and crucial) modification is to replace the free electron mass in Eqs. (6) and (7) by the effective mass associated to the material  $m^*$ . This requires a redefinition of the parameter  $x$  as well, namely,

$$x = \left(\frac{\lambda}{d}\right) \left(\frac{m}{m^*}\right) \sqrt{\frac{I}{n_r I_C}}. \quad (10)$$

For a specific application, let us assume a CO<sub>2</sub> laser with  $\lambda = 10.6\mu\text{m}$  ( $\hbar\omega = 117\text{meV}$ ) and a *GaAs-Al<sub>x</sub>Ga<sub>1-x</sub>As* ( $x \approx 0.3$ ) heterostructure of lattice constant  $d = 76\text{\AA}$ . This choice leads to  $\hbar\omega = 0.3\epsilon$ . The other parameters take the values  $m^* \approx 0.067m$ ,  $n_r \approx 3.4$ ,  $\epsilon \approx 390\text{meV}$ ,  $\sigma \approx 97\text{meV}$ , and  $I_C \approx 1.2 \times 10^{16} \text{ W/cm}^2$ . We thus find the relation

$$x^2 \approx \frac{I}{9.4 \times 10^7 \text{ W/cm}^2}. \quad (11)$$

Under these conditions, the laser intensity necessary to produce strong coupling, namely,  $x \approx 10$ , is of the order of  $10^{10} \text{ W/cm}^2$ . Such intensity is experimentally accessible and does not cause irreversible damage to the heterostructure [11]. Nevertheless, one should have in mind that not all parameters are fixed by the choice of lattice constant and laser frequency. The well width can still be chosen independently (implying in a modification of the ratio  $\sigma/\epsilon$ ). The values chosen above only represent the strong mixing (chaotic) situation compatible with our numerical simulations. Of course, decreasing the intensity would make the system no longer chaotic.

We believe that the transition between regular and chaotic behaviors can manifest itself in at least two ways. As previously discussed, the onset of chaos is related to a narrowing of the electronic bands, causing a decrease in the mobility along the superlattice direction. As

a result, transport measurements should reveal a maximum of the transverse conductivity when the laser intensity is small. Another effect of chaos appears in the strong mixing between energy bands. Optical transitions which were initially forbidden when no light is shone into the heterostructure should become observable at high laser field intensities. One could, in principle, irradiate the superlattice with a pump laser and measure the intensity of a large set of these new absorption lines using a second (much weaker) probe laser [11]. The histogram of oscillator strengths thus generated should fall into a universal curve predicted by random matrix theory [12] when  $x \approx 10$ .

## V. CONCLUSIONS

We have studied the interaction of a quantized laser field with an electron in a 1-D lattice. The classical dynamics of Hamiltonian which describes the problem was analyzed through the stroboscopic map technique. We found that a transition from regular to chaotic motion can be obtained by increasing the laser field intensity. The main signature of such transition would be a large change in the electron mobility, leading to a suppression of charge conductance in the irradiated material. An experimental realization of the model is a laser interacting with a superlattice. The conditions which must be fulfilled for the laser and the lattice parameters are compatible with the experimental possibilities. This implies the use of infrared lasers and superlattices of periodicity around 100Å.

## ACKNOWLEDGMENTS

This work was partially supported by the Brazilian agencies Conselho Nacional de Desenvolvimento Científico e Tecnológico (CNPq), Financiadora de Estudos e Projetos (FINEP), and Fundação Universitária José Bonifácio (FUJB-UFRJ).

## REFERENCES

- [1] M. C. Gutzwiller, *Chaos in Classical and Quantum Mechanics* (Springer, New York, 1990); F. Haake, *Quantum Signatures of Chaos* (Springer, Berlin, 1991); *Chaos and Quantum Physics*, edited by M.-J. Giannoni, A. Voros, and J. Zinn-Justin (North-Holland, Amsterdam, 1991).
- [2] G. Casati, B. V. Chirikov, F. M. Izrailev, and J. Ford, in *Stochastic Behavior in Classical and Quantum Hamiltonian Systems*, edited by G. Casati and J. Ford (Springer, Berlin, 1979).
- [3] F. L. Moore, J. C. Robinson, C. Bharucha, P. E. Williams, and M. G. Raizen, Phys. Rev. Lett. **73**, 2974 (1994); J. C. Robinson, C. Bharucha, F. L. Moore, R. Jahnke, G. A. Georgakis, Q. Niu, M. G. Raizen, and B. Sundaram, Phys. Rev. Lett. **74**, 3963 (1995); P. J. Bardsroff, I. Bialynicki-Birula, D. S. Krahmer, G. Kurizki, E. Mayr, P. Stifter, and W. P. Schleich, Phys. Rev. Lett. **74**, 3959 (1995).
- [4] H. Hasegawa, M. Robnik, and G. Wunner, Prog. Theor. Phys. Suppl. **98**, 198 (1989); H. Friedrich and D. Wintgen, Phys. Rep. **183**, 37 (1989).
- [5] N. Tzoar and J.I. Gersten, Phys. Rev. B **12**, 1132 (1975); G. Jalbert, B. Koiller, H.S. Brandi, and N. Zagury, J. Phys. C **19**, 5745 (1986).
- [6] H. S. Brandi *et al.*, Quim. Nova **11**, 102 (1988).
- [7] M. L. Mehta, *Random Matrices*, 2nd ed. (Academic Press, San Diego, 1991).
- [8] Due to inversion symmetry of the lattice unit cell, there is a *false* time-reversal symmetry violation in the Hamiltonian (6) and the correct Gaussian ensemble to compare with is the *orthogonal* one. See discussion in M. Robnik and M. V. Berry, J. Phys. A: Math. Ge. **19**, 669 (1986).
- [9] M. A. M. de Aguiar, K. Furuya, C. H. Lewenkopf, and M. C. Nemes, Ann. Phys. (NY) **216**, 291 (1992)].
- [10] L. Esaki and R. Tsu, IBM J. Res. Dev. **14**, 61 (1970).
- [11] A. Mysyrowicz, D. Hulin, A. Antonetti, A. Migus, W. T. Masselink, and H. Morkoç, Phys. Rev. Lett. **56**, 2748 (1986).
- [12] N. Taniguchi and V. N. Prigodin, Phys. Rev. B **54**, R14305 (1996).

## FIGURES

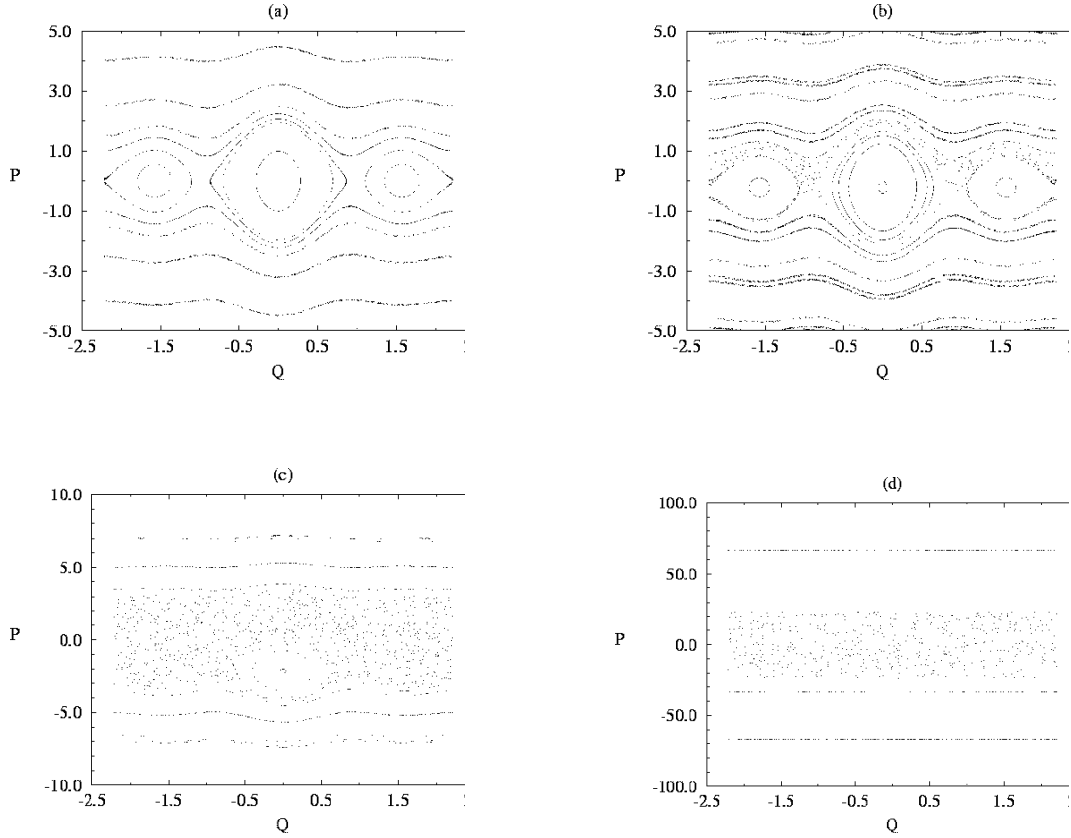


FIG. 1. Stroboscopic maps of the Hamiltonian in Eq. (3) for (a)  $x = 0$ , (b)  $x = 1$ , (c)  $x = 10$ , and (d)  $x = 100$ . See the text for a discussion.

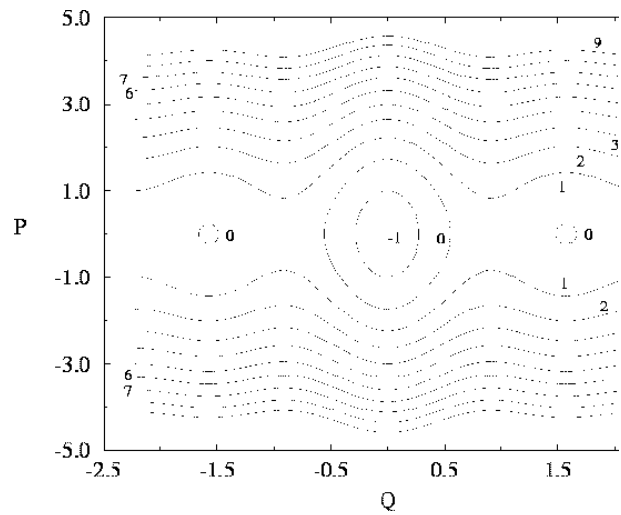


FIG. 2. Contour plots of the Hamiltonian in Eq. (3) for  $x = 0$ .

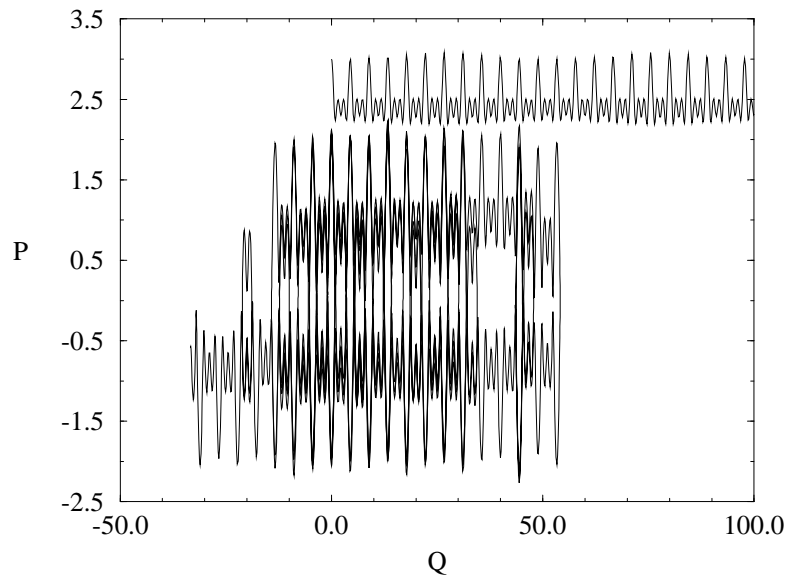


FIG. 3. Classical electron trajectories for  $x = 1$ . The upper curve is a regular trajectory for the initial conditions  $Q = 0$ ,  $P = 3$  and propagation time = 50. The lower curve is a chaotic trajectory for the initial conditions  $Q = 0$ ,  $P = 1.9$  and propagation time = 500.

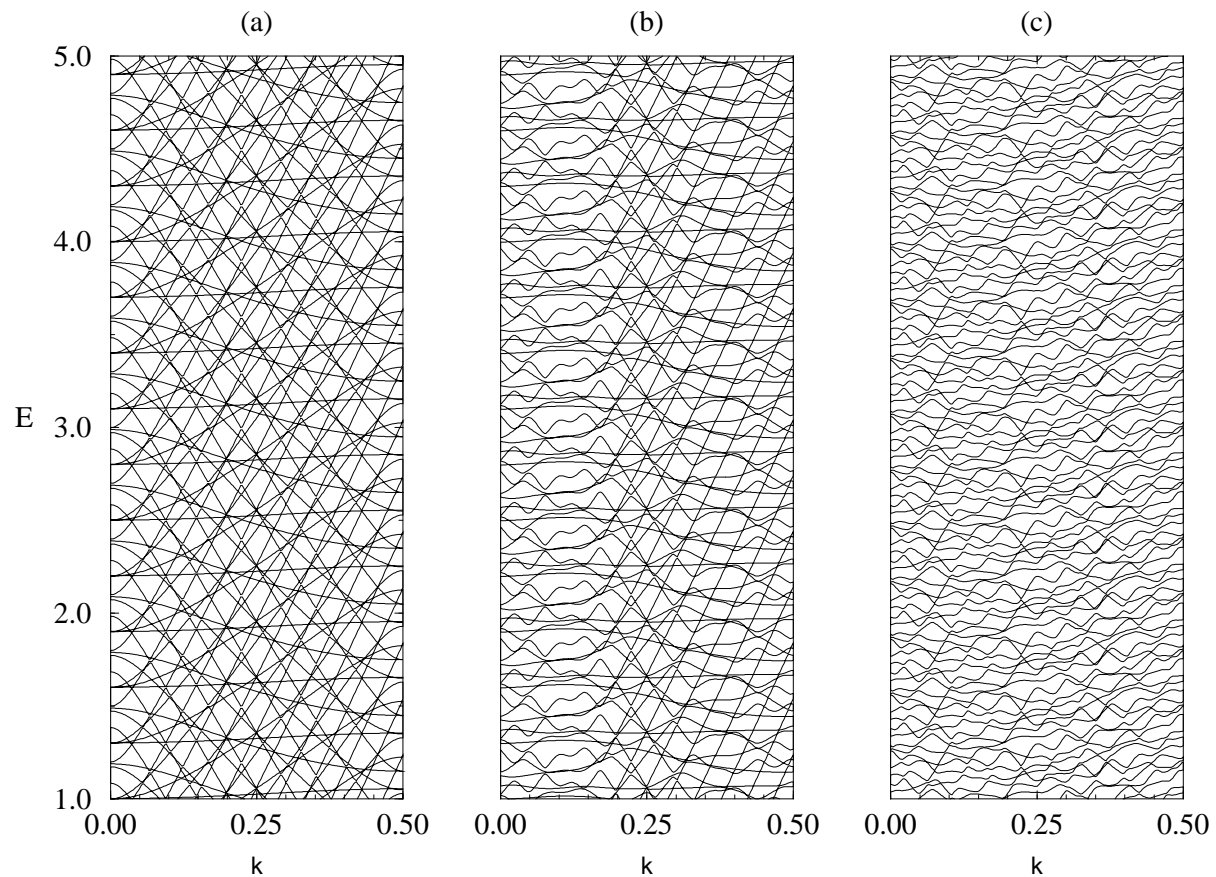


FIG. 4. Energy bands for (a)  $x = 0$ , (b)  $x = 1$ , and (c)  $x = 10$  calculated with parameters  $\ell_{\max} = 3$  and  $n_{\max} = 40$ .

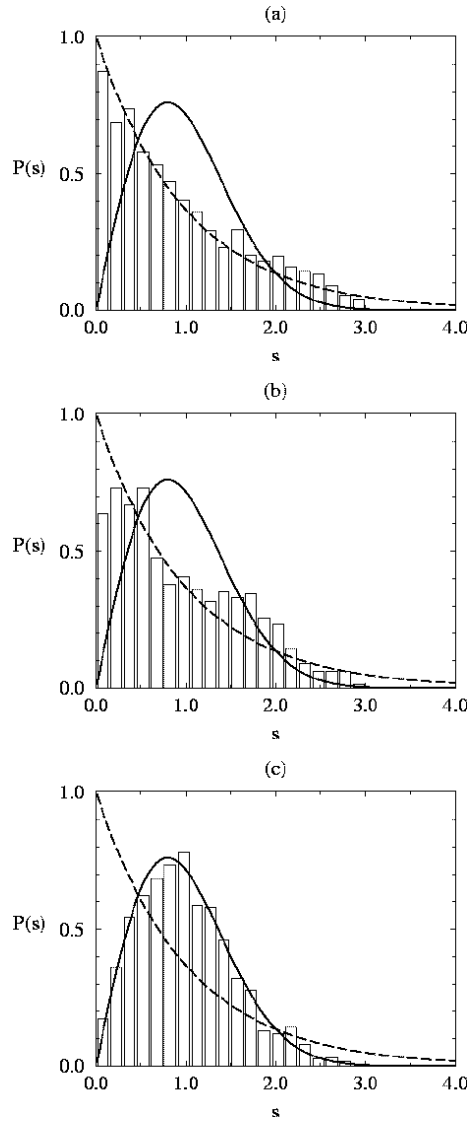


FIG. 5. Nearest neighbors statistics (NNS) for (a)  $x = 0$ , (b)  $x = 1$ , and (c)  $x = 10$  for  $\ell_{\max} = 3$  and  $n_{\max} = 40$ . The dashed lines are Poissonian distributions while the solid lines correspond to GOE distributions of level spacings.

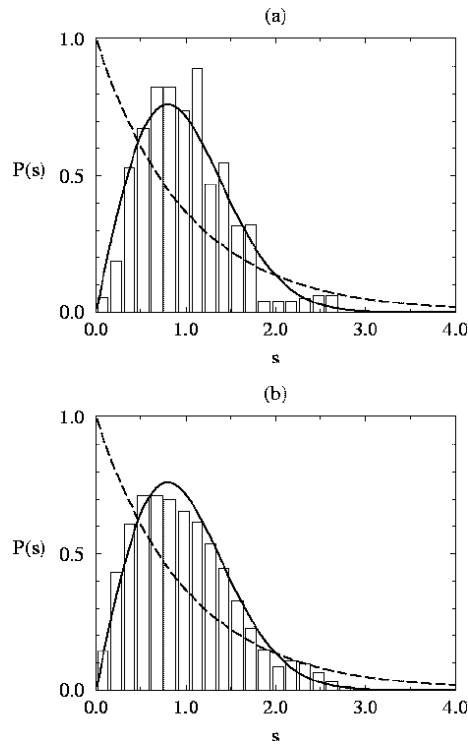


FIG. 6. Dependence of the nearest neighbors statistics (NNS) for  $x = 10$  on the number of plane waves  $\ell_{\max}$ . The histograms correspond to (a)  $\ell_{\max} = 1$ ,  $n_{\max} = 40$ , and (b)  $\ell_{\max} = 5$ ,  $n_{\max} = 60$ , i.e., 3 and 11 electronic bands models, respectively. These results, together with Figure 5(c), illustrate the robustness of our results with respect to the basis set truncation parameters.